Int. J. Electrochem. Sci., 17 **(2022)** Article Number: 220439, doi: 10.20964/2022.04.23

International Journal of
ELECTROCHEMICAL
SCIENCE
www.electrochemsci.org

Novel Electrochemical Immunosensor Based on an Abs-AuNPs@ZIF-67 Probe for the Simultaneous Detection of Fenpropathrin and Deltamethrin in Vegetables

Yaodong Xiang[1], Haowei Dong[1], Rui Xu[1], Jingcheng Huang[1], Guangxian Wang[1], Fukai Guan[1], Honggang Fang[1], Yemin Guo[1,], Mohamed Bedair Mohamed Ahmed[2,*]*

[1] School of Agricultural Engineering and Food Science, Shandong University of Technology, No. 266 Xincun Xilu, Zibo 255049, China
[2] Food Toxicology and Contaminants Dept, Division of Food Industries and Nutrition, National Research Centre, 33 El-Bohouth St, Dokki, Cairo 12622, Egypt
[*]E-mail: gym@sdut.edu.cn; md.bedair@nrc.sci.eg

Received: 11 December 2021 / *Accepted:* 28 January 2022 / *Published:* 4 March 2022

To solve the problem of uniform immobilization of gold-labelled antibodies on an electrode surface, an antibody-labelled Abs-AuNPs@ZIF-67 probe was synthesized by a one-step wet chemical method, and an electrochemical immunosensor based on gold-labelled antibody probes for the detection of pyrethroid (PYR) pesticides was constructed. This method enhanced the uniform dispersion effect of gold-labelled antibodies on the electrode surface and improved the immobilization level of broad-spectrum antibody. The detection ranges for fenpropathrin and deltamethrin were determined to be 0.286-2.864 × 10^5 nM and 1.979-1.979 × 10^5 nM, with linear correlation coefficients of 0.9941 and 0.9874, respectively. The limits of detection for fenpropathrin and deltamethrin were determined to be 0.0258 nM and 1.712 nM, respectively. This detection method was compared with the standard GC-MS method for the determination of PYRs in vegetable samples. The electrochemical immunosensor showed a high recovery rate (93.69%-102.11%) in a spiked sample recovery experiment. The constructed electrochemical immunosensor shows high sensitivity, selectivity and stability. This study not only provided a new gold-labelled antibody probe for the rapid detection of fenpropathrin and deltamethrin but also provided a new pathway for the construction of electrochemical immunosensors for the detection of other pesticides and small molecule targets.

Keywords: Gold-labelled antibody probes, Fenpropathrin, Deltamethrin, Electrochemical immunosensor, Broad-spectrum antibodies, Synthetic pyrethroids.

1. INTRODUCTION

Pyrethroids (PYRs) are highly toxic and rapid insecticides. Their widespread use can easily lead to residues, causing tremor syndrome and allergic reactions in humans[1, 2]. Fenpropathrin and

deltamethrin pesticide residues in fruits and vegetables can affect human health and cause problems related to PYR accumulation in the environment. Therefore, it is urgent to develop an economical and reliable method suitable for field application. It is particularly important to develop a small molecule target detection method for the sensitive detection of fenpropathrin and deltamethrin pesticides[3].

At present, the detection methods for PYRs include enzyme-linked immunosorbent assay[4, 5] fluorescence analysis[6], chemiluminescence[7] and electrochemical immunosensors[8]. However, the application of enzyme-linked immunosorbent assay (ELISA) in the rapid detection of pesticide residues in vegetables is limited due to the high cost of antibody preparation and sample detection. Fluorescent colorimetry is easily disturbed by pigments in vegetable matrices, which affects its accuracy. Electrochemical immunosensors use the specific binding mechanism between antibodies to identify targets to change the conformation of antibodies and the current signal on the electrochemical sensing interface. Electrochemical biosensors have become a research hotspot in recent years due to their advantages of high sensitivity, fast signal response and easy equipment miniaturization[9-13].

To sensitively detect PYRs and build an efficient recognition element for electrochemical immunosensors, a signal amplification platform with a large specific surface area, good biocompatibility and excellent detection performance is required[14]. Noble metal materials and transition metal alloys have good biocompatibility, large specific surface area and electrical conductivity and are widely used in the preparation of immunosensors, especially gold-labelled antibodies[15-17]. Metal-organic frameworks (MOFs) with extremely high surface areas and high porosities are considered potential supporting materials for the fabrication of immunosensors loaded with nanoparticle[18-21]. ZIF-67 prepared by one-step wet chemical synthesis in this study has a regular dodecahedron structure and a large specific surface area, which provides abundant surface active sites for the attachment of gold-labelled antibodies. ZIF-67 (MOF) shows great potential for constructing sensitive electrochemical immunosensors[22-26]. Reduced graphene oxide (rGO) is the product of graphite oxidation stripping and reduction, and the structure of rGO is very similar to GO. Compared with GO, rGO has better conductivity and is easier to disperse, manipulate and prepare. rGO can be directly introduced into the preparation of the electrochemical sensing interface. Its good electrical conductivity and electrochemical sensing activity has led to its wide use as a sensor substrate material in electrochemical applications[27-29].

In brief, we consider the construction of an electrochemical immunosensor for the simultaneous detection of fenpropathrin and deltamethrin and the synthesis of a gold-labelled Abs-AuNPs@ZIF-67 probe by a one-step wet chemical synthesis. The prepared AuNPs@ZIF-67 nanocomposite shows good stability, enhances the uniform dispersion effect of the electrode surface, and overcomes the previous agglomeration problem for antibody probes on the electrode surface.

2. EXPERIMENT

2.1 Reagent

A glassy carbon electrode (GCE, GaossUnion), saturated calomel electrode (SCE, GaossUnion), and platinum electrode (PtE, GaossUnion) were used as the working electrode, reference electrode and

counter electrode, respectively, in the three-electrode platform system of the electrochemical sensor. $Co(NO_3)_2 \cdot 6H_2O$, bovine serum albumin (BSA), and 1,2-dimethylimidazole were obtained from Sigma-Aldrich (USA). The reagents used in the whole process, such as $HAuCl_4 \cdot 3H_2O$, $C_6H_5O_7Na_3$, $NaBH_4$, K_2CO_3, H_3BO_3, $K_3[Fe(CN)_6]$, NaOH and other chemical reagents, were at the analytical level. The monoclonal antibodies (Abs) against PYR as the key recognition components were supplied by Beijing Biodragon Immunotechnologies Co., Ltd. The graphene oxide (GO) was procured from Nanjing XFNANO Materials Tech Co., Ltd. Deltamethrin and fenpropathrin, permethrin, profenofos, isocarbophos, acetamiprid and imidacloprid were supplied by Beijing Yihuatongbiao Technology Co., Ltd.

2.2. Instrument

The resistivity of the ultra-pure water used in this work was standard 18.2 MΩ·cm (Milli-Q system, Millipore, USA). The operation of the electrochemical immunosensor was realized in an electrochemical workstation (CHI660D, Shanghai Chenhua Co., Ltd., China). The FT-IR spectra were acquired using an FT-IR spectrometer (Nicolet 5700, Thermo Scientific, USA). The UV-Vis spectra for GO and rGO were measured by a multifunction microplate reader (Varioskan LUX, Thermo Scientific, USA). The Abs-AuNPs@ZIF-67 was prepared by a centrifuge machine (ST16R, Thermo Scientific, USA). TEM, STEM and EDS characterization of AuNPs and Abs-AuNPs@ZIF-67 was performed by transmission electron microscopy (Tecnai G2 Spirit TWIN, USA). The surface morphologies of rGO and Abs-AuNPs@ZIF-67/rGO were determined by field emission scanning electron microscopy (FE-SEM, Quanta 250, FEI, USA). The Raman spectra for the samples were measured using a high-resolution Raman spectrometer (HORIBA JY, France).

2.3 Preparation of the electrochemical immunosensor

2.3.1 Preparation of Abs-AuNPs@ZIF-67 antibody probes

AuNPs were prepared according to the method of Dong [30] by trisodium citrate reduction. The AuNPs@ZIF-67 composites were synthesized by a one-step wet-chemical approach, schematically illustrated in Scheme S1, Text S1. A 10 ml mixed solution containing 33.6 mmol (2.76 g) of 2-methylimidazole in methanol was prepared. The prepared AuNPs solution with a particle size of about 12 nm was centrifuged and concentrated (12,000 rpm) to 10%. The first two mixed solutions were evenly mixed for preparation using a magnetic stirrer. $Co(NO)_3 \cdot 6H_2O$ (1.6 mmol, 0.46 g) was added to 12 mL methanol (solution B), and solution A and solution B were mixed together slowly and evenly and reacted at room temperature for 3 h (400 rpm). The reaction was synthesized by a one-step wet chemical method, centrifuged with AuNPs@ZIF-67, and then stored at 4°C. Then, 180 μL $K_2CO_{30.}$ (1 M) solution was added to 10 mL AuNPs@ZIF-67, and AuNPs@ZIF-67 was coupled with Abs in order to form an alkaline environment. Then, 0.1 mg/mL of PYR broad-spectrum antibody (600 μL) was added and oscillated at 25°C for 30 min to ensure that positive charge cluster around the antibody protein formed a firm bond with the negative charge around the gold nanoparticle through electrostatic adsorption. BSA (1,190 μL,

10%, m/v) was added to seal the nonspecific binding sites by oscillating the reaction for 30 min. After incubation at 4℃ for 3 h, the supernatant was discarded after centrifugation (4,000 rpm, 5 min). Then, 1,000 μL of borate buffer solution (2.0 mM) was added and the mixture shaken until uniform. The above operation was repeated and saved at 4℃.

2.3.2 Preparation of substrate materials (rGO)

First, GO solution (100 mg) was prepared in 100 mL ultra-pure water, and an ultrasonic bath was conducted for 30 min to evenly disperse the GO colloid. After adding 1 mol/L NaOH solution to adjust the pH of the dispersant to 9.5, 800 mg $NaBH_4$ was dispersed in 100 mL GO dispersant and stirred at 90℃ for 1 h. When $NaBH_4$ was added, the brown dispersion immediately turned black, indicating an increase in rGO content[27]. Finally, ultra-pure water was used to filter and wash the dispersion.

2.3.3 Preparation of the Abs-AuNPs@ZIF-67/rGO/GCE immunosensor

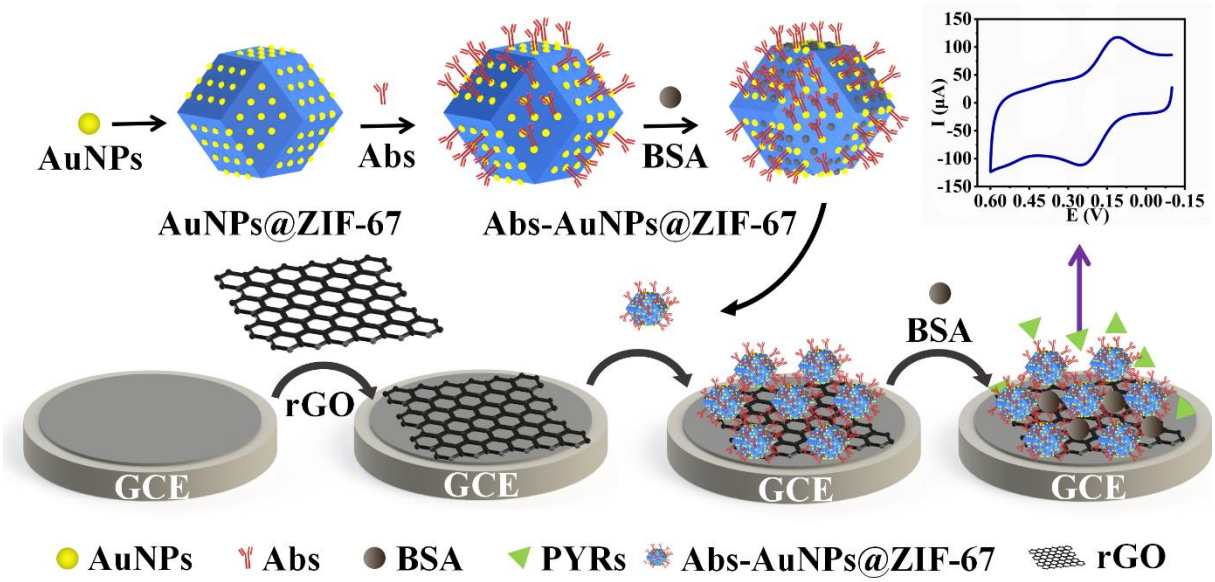

Scheme 1. Schematic illustration for the fabrication of the electrochemical immunosensor.

Scheme 1 shows a schematic diagram of the label-free electrochemical immunosensor fabricated on the GCE. First, the GCE was cleaned by polishing with alumina powder and ultrasonication in a mixture of water and ethanol. An aliquot of rGO dispersed sample (8 μL) was immobilized onto the cleaned GCE surface as substrate material. An aliquot of gold-labelled antibody probe (Abs-AuNPs@ZIF-67) dispersed sample (8 μL) was mounted onto the substrate material surface. The modified electrode was dried at room temperature for 30 min.

Then, the nonspecific binding site was blocked and the modified electrode was blocked with 8 μL BSA (0.5 wt %) solution for 30 min. Finally, 8 μL PYRs were added to the surface of the modified electrode and incubated at 37℃ for 50 min. This modified GCE constituted the working electrode and

was used for further experimental studies.

2.4 Electrochemical detection methods

With the construction of the electrochemical immunosensor for PYR detection, the electrochemical behavior of the electrode surface changed. To investigate and analyze this change, cyclic voltammetry (CV) scanning was performed in $[Fe(CN)_6]^{3-/4-}$ solution (pH 7.4, 5.0 mM). The potential parameter range for electrochemical scanning was set as -0.1 V to + 0.6 V, and the standard scanning rate was 0.05 V/s. . In this process, two kinds of electrochemical immunosensors were prepared under the best experimental conditions, and their CV electrochemical response values were measured. The CV response values for each electrochemical immunosensor after BSA blocking were measured and denoted as I_1. After the surface of the electrode was washed and blow-dried, the CV response value of the electrode of the electrochemical immunosensor after adding the PYR-containing solution was collected and denoted as I_2. After calculating the ΔI value ($\Delta I=I_2-I_1$), the relationship between ΔI and the PYR concentration was analyzed.

2.5 Pretreatment of samples

Samples of lettuce and baby cabbage purchased from a market were crushed into slurries, and each sample (50.0 g) was accurately weighed. Each solution was extracted with 160.0 mL methanol-PBS (70%, v/v) and then mixed for 2 min. After homogenization, the subsequent experimental solution was formed after filtration with a 0.45 μm filter membrane.

3. RESULTS AND DISCUSSION

3.1 Characterization of Abs-AuNPs@ZIF-67/rGO/GCE

3.1.1 Characterization of AuNPs

Field emission transmission electron microscopy (FE-TEM) images (Figure 1B) show that the AuNP samples present a face-centred cubic (FCC) lattice with an Au interlayer spacing of 0.24830 nm. The prepared AuNPs show a globular shape (Figure 1A) and uniform distribution (Figure 1C and 2D). Figure 1D confirms the homogeneous distribution of AuNPs with an average size of approx. 10-12 nm. The morphology of the prepared nanostructures was revealed by FE-TEM images, indicating that the AuNPs were well prepared.

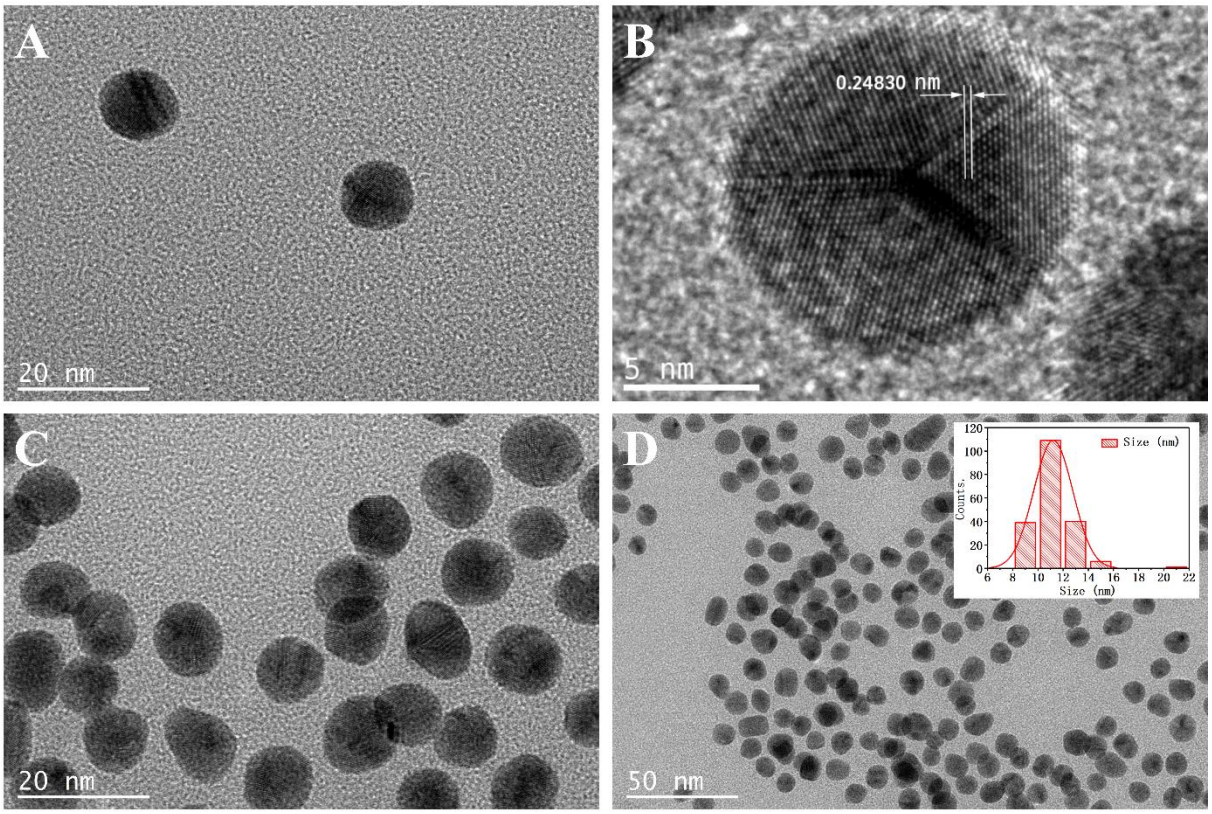

Figure 1. FE-TEM images of the AuNPs (A), (B), (C), (D) at different magnifications; FE-TEM images representing the lattice size of the AuNPs (B); FE-TEM image of the size distribution of the AuNPs (D).

3.1.2 Characterization of gold-labelled antibody probes (Abs-AuNPs@ZIF-67)

UV-Vis absorption spectroscopy was used to evaluate the combining ability of the AuNPs, AuNPs@ZIF-67 and Abs-AuNPs@ZIF-67. Figure 2 shows the UV-Vis absorption spectra for conventional gold-labelled antibody probes. The UV-Vis spectrum for AuNPs is shown in Figure 2A-a. At a wavelength of 522 nm, a strong plasma absorption peak induced by collective electron oscillations was observed for the 12 nm AuNPs. Figure 2A-b show UV-Vis absorption spectra for AuNPs bound to Abs protein. After modification by Abs, the plasma absorption peak for the AuNPs showed a redshift from 522 nm to 537 nm. The resonant wavelength and bandwidth of the AuNPs were related to the particle size and shape, refractive index and temperature of the surrounding medium. This change is attributed to the change in the dielectric properties around the Abs-AuNPs after the conjugation of AuNPs and Abs[31, 32].

Figure 2B shows the UV-Vis absorption spectra for the gold-labelled antibody probes used in this study. Figure 2B-c shows the UV-Vis absorption spectra for ZIF-67. Figure 2B-d shows the UV-Vis absorption spectra for the AuNPs. Figure 2B-b shows the UV-Vis absorption spectra for Abs protein-stabilized AuNPs@ZIF-67. The optical properties of AuNPs@ZIF-67 showed one peak at 586 nm, which could be related to the $^4A_2(F) \rightarrow {}^4T_1(P)$ transition and the metal-ligand charge transfer (MLCT) for Co(II) ions. The plasma absorption peak for the gold-labelled antibody probe shifted from 522 nm to

534 nm after the modification of the antibody, similar to the shift observed for of the conventional gold-labelled probe from 522 nm to 537 nm. This shift after conjugation of AuNPs@ZIF-67 with Abs was attributed to the changes in the dielectric nature surrounding the AuNPs@ZIF-67 due to the presence of Abs. The above analysis characterized the successful preparation of gold-labelled antibody probes[32].

Figure 2C shows the Raman spectra for the prepared GO and rGO. This figure shows obvious Raman characteristic vibration peaks for the D-band (A1g) and G-band (E2g) of graphene at 1349.86 cm^{-1} and 1597.33 cm^{-1}[33], and the D-band and G-band of rGO at 1345.09 cm^{-1} and 1597.33 cm^{-1}, respectively[34]. The GO I_D/I_G value is smaller than the rGO I_D/I_G value. Figure 2D shows the FT-IR spectra for GO and rGO. It can be observed from the figure that a large number of functional group peaks appear on GO within the detected wavelength range.

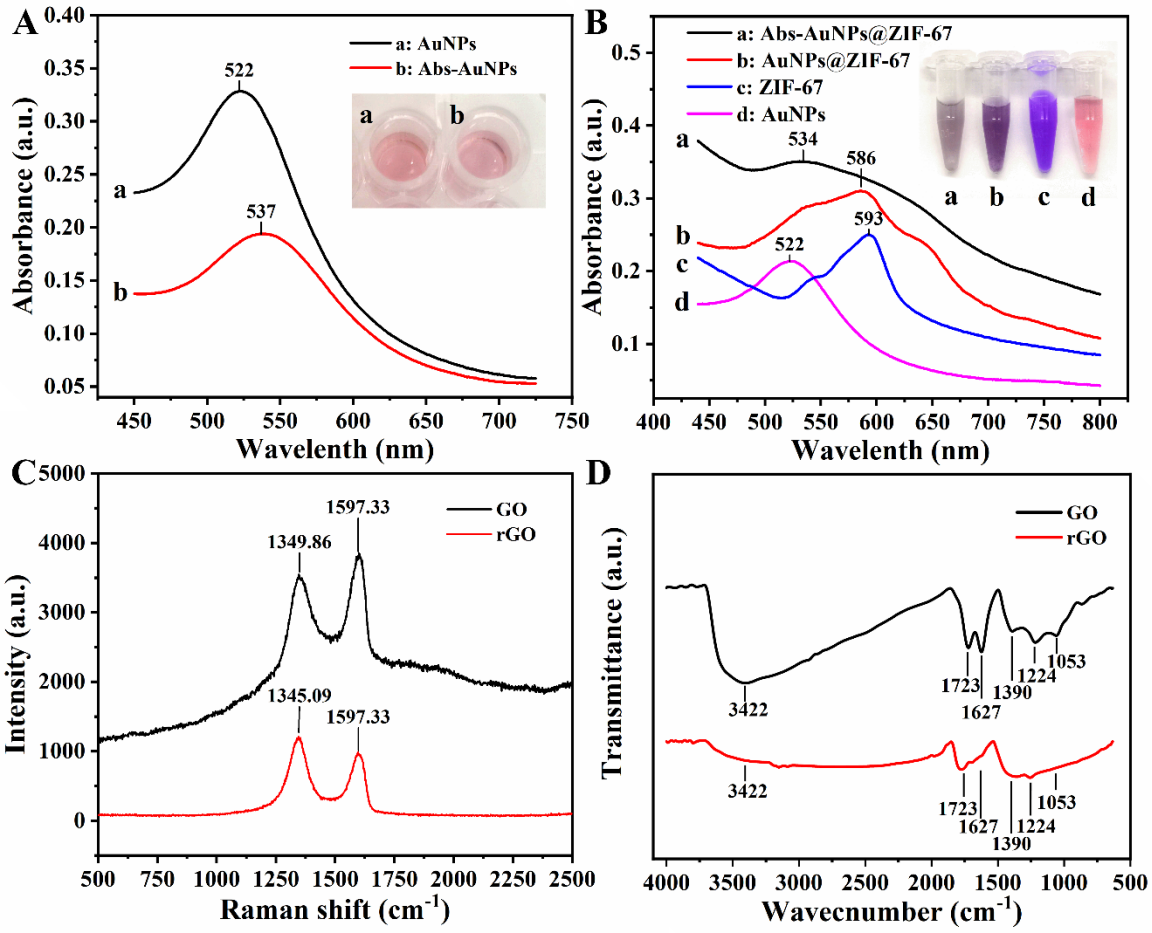

Figure 2. UV-Vis absorption spectra for gold-labelled antibody probes (A), (B). Raman spectra for GO and rGO (C). FT-IR spectra for GO and rGO (D).

The strong absorption peaks observed at 3422 cm^{-1} and 1053 cm^{-1} were attributed to the stretching vibration of hydroxyl groups in the GO plane, the stretching vibration peak of C=O at 1723 cm^{-1}, the characteristic stretching vibration peak of C=C at 1627 cm^{-1} and 1224 cm^{-1}, and the stretching vibration peak of carboxyl C-OH at 1390 cm^{-1}. This indicates that GO contains functional groups such as hydroxyl and carboxyl groups[33]. However, the stretching vibration peaks for rGO in different

functional groups shows a significant decrease, indicating that a large number of functional groups were reduced after GO was reduced to rGO. The Raman spectra and the FT-IR spectra proved that the rGO in the constructed electrochemical immunosensor was successfully synthesized.

3.1.3 Characterization of Abs-AuNPs@ZIF-67/rGO

AuNPs on ZIF-67 were observed by field emission transmission electron microscopy (FE-TEM). The TEM, SEM and STEM results show that AuNPs were dispersed and spherical and ZIF-67 has a regular dodecahedron structure (Figure 3A and 3B) with an average particle size of 200 nm.

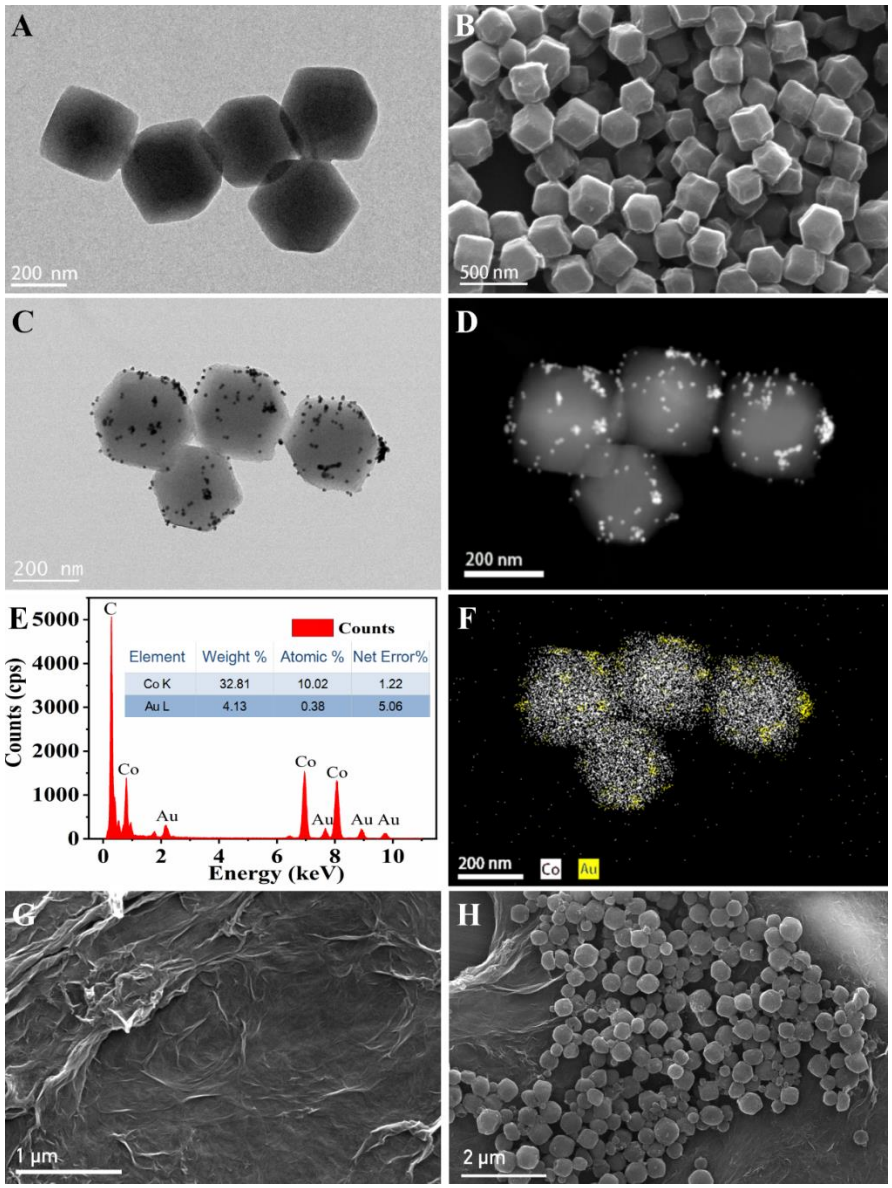

Figure 3. FE-TEM images for ZIF-67 (A). FE-SEM images for ZIF-67 (B). FE-TEM images for Abs-AuNPs@ZIF-67 (C). STEM images for Abs-AuNPs@ZIF-67 (D). EDX spectra for Abs-AuNPs@ZIF-67 (E). Elemental mapping for Co and Au (F). FE-SEM images for rGO (G). FE-SEM images for Abs-AuNPs@ZIF-67/rGO (H).

Figure 2 shows the successful binding of AuNPs to ZIF-67, while scanning transmission electron microscopy (STEM, Figure 3D) shows the complete fusion of AuNPs and ZIF-67. AuNPs were uniformly adhered to the surface of ZIF-67 without a clear boundary. The presence of AuNPs in the composites was confirmed by energy spectral analysis (EDS) of AuNPs@ZIF-67 (Figure 3C and 3E) and the element distribution mapping phase (Figure 3F), which shows that the composites were composed of Au and Co. To intuitively understand the nanostructure of the AuNPs@ZIF-67 samples, STEM tests were performed. More importantly, the STEM maps for Co and Au were found to match well with the dispersive spectroscopy (EDS) analysis of Co and Au in AuNPs@ZIF-67, indicating that AuNPs were uniformly loaded and compacted in ZIF-67. TEM characterization of Abs-AuNPs@ZIF-67/rGO and rGO-modified electrodes shows that Abs-AuNPs@ZIF-67 probe was uniformly immobilized on the surface of rGO-modified electrode.

3.2 Optimization of the immunosensor conditions

To explore the optimal immunosensor performance, different experimental parameters were systematically studied in this work. Figure 4A shows the effect of the coupling rate between the antibody and AuNPs on the immunosensor performance, which influenced the charge transfer efficiency of the electrode interface. The coupling efficiency between AuNPs and antibody has an important influence on electrochemical immunosensor detection. We know that an increased number of antibodies on the sensor surface can increase the sensitivity of the test but will also increase in the cost of the test. At the same time, the electrical conductivity of Abs-AuNPs is decreased by the coupling of too many antibodies. In this work, the effects of coupling different concentrations of antibody and AuNPs on the conductivity of the sensor interface were studied. The redox capacity of $[Fe(CN)_6]^{3-/4-}$ the interface of the electrochemical immunosensor was measured by the CV method. When the concentration of the antibody was 6.0 μg/mL, a larger ΔI value was obtained (Figure 4A). The minimum average deviation was obtained at this concentration, indicating that the electrochemical immunosensor prepared under this condition has the best stability. Therefore, 6.0 μg/mL was selected as the optimal antibody concentration.

Second, the effect of the incubation time was was studied to establish the minimum immuno-reaction time that assures the interaction between the Abs-AuNPs@ZIF-67 on the immunosensor surface and the PYRs. The incubation times were 25 min, 30 min, 35 min, 40 min and 45 min. When the target pesticide was present in solution, the PYRs-Abs complex was formed at the immunosensor interface, weakening the electron transfer ability and resulting in a decrease in the peak current. The incubation time of the antibody was also very important for the performance of the immunosensor. A short time might not allow the target pesticide to fully bind to the antibody, while an extended time might lead to the inactivation of the antibody to a certain extent. The number of complexes was correlated with the specific recognition time of the PYR pesticide small molecule and the gold-labelled antibody. Therefore, the specific recognition between gold-labelled antibodies and PYR pesticides is affected by the reaction time. Over time, an increasing number of pesticide molecules wre captured on the surface of the electrode, resulting in electron transfer and a gradual increase in ΔI (Figure 4B). When the critical point

was reached (40 min), the sensor surface compounds reached saturation. The ΔI values did not change significantly when the culture time was further increased. Therefore, 40 min was chosen as the best incubation time for the immunosensor and pesticide target.

In addition, the pH value of the buffer solution is a necessary condition for electrochemical immunosensors, because it affects the biological activity of the antibody and the electrochemical performance of electrochemical immunosensors. On this basis, a series of potassium ferricyanide solutions with pH 6.0-9.0 were selected as the experimental conditions. As shown in Figure 4C, the electrochemical signal response of the electrochemical immunosensor increased with a change in pH value from 6.0 to 7.5, reaching the maximum signal response at 7.5, and then decreased with a further increase in pH value.

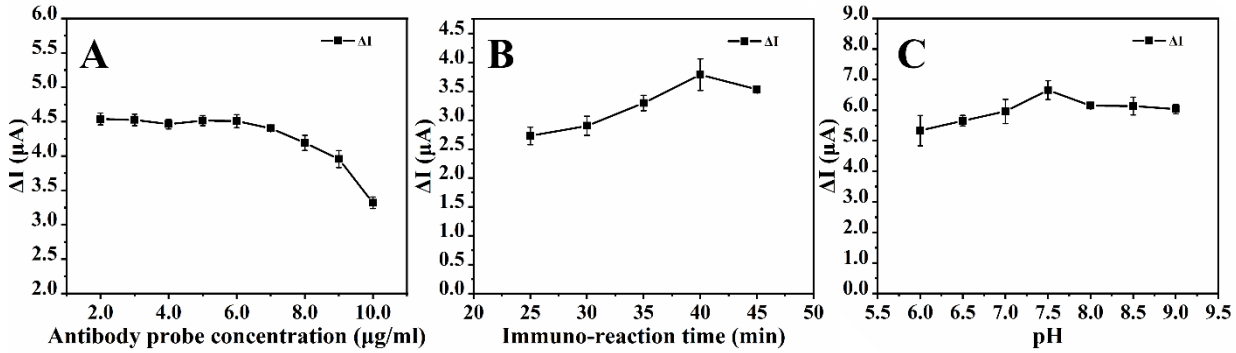

Figure 4. Optimization of the experimental parameters for the electrochemical immunosensor sensor: (A) Antibody probe concentration; (B) Incubation time; (C) pH value.

3.3 Electrochemical detection of PYRs

As shown in Figure 5A, we used CV to evaluate the electrochemical characteristics of the electrochemical immunosensor. The CV electrochemical spectrum shows a pair of reversible redox peaks on the bare electrode sensor surface (e). After rGO was modified on the electrode surface, the peak current for the electrode shows a significant increase due to the good conductivity of rGO (d). When the rGO substrate was modified by Abs-AuNPs@ZIF-67, the peak current was reduced. The decrease in the peak current of the electrode (c) was due to the organometallic frame structure and gold-labelled antibody modification on its surface, which reduced the conductivity of the sensing interface. When BSA was added to the surface of the electrochemical immunosensor to block nonspecific sites, the peak current of the immunosensor continued to decrease (b). With the addition of PYRs, the peak electrode current decreased again (a), and the formation of complexes between PYRs and Abs further limits the electron transfer ability in the system.

Electrochemical impedance spectroscopy (EIS) is an efficient method for detecting the interface properties of sensors by setting Nyquist plots for each surface modification step, helping to assess the charge transfer coefficient[35, 36]. ZView software was used for circuit fitting of the Randle equivalent circuit, as shown in Figure 5B. The diameter of the semicircle in the EIS impedance characterization

diagram represented the charge transfer resistance (Rct). The Rct for rGO/GCE (d) was higher than that for GCE (e), indicating that rGO promoted electron transfer during the electrode reaction. The Rct value (c) for the electrode modified with the gold-labelled antibody probe was significantly larger than that for rGO/GCE. When BSA (b) and PYRs (a) were further modified on the electrode, the Rct showed a successive increase. The EIS and CV spectra measured for the sensor in this experiment were consistent. These results demonstrate the successful assembly of the electrochemical immunosensor.

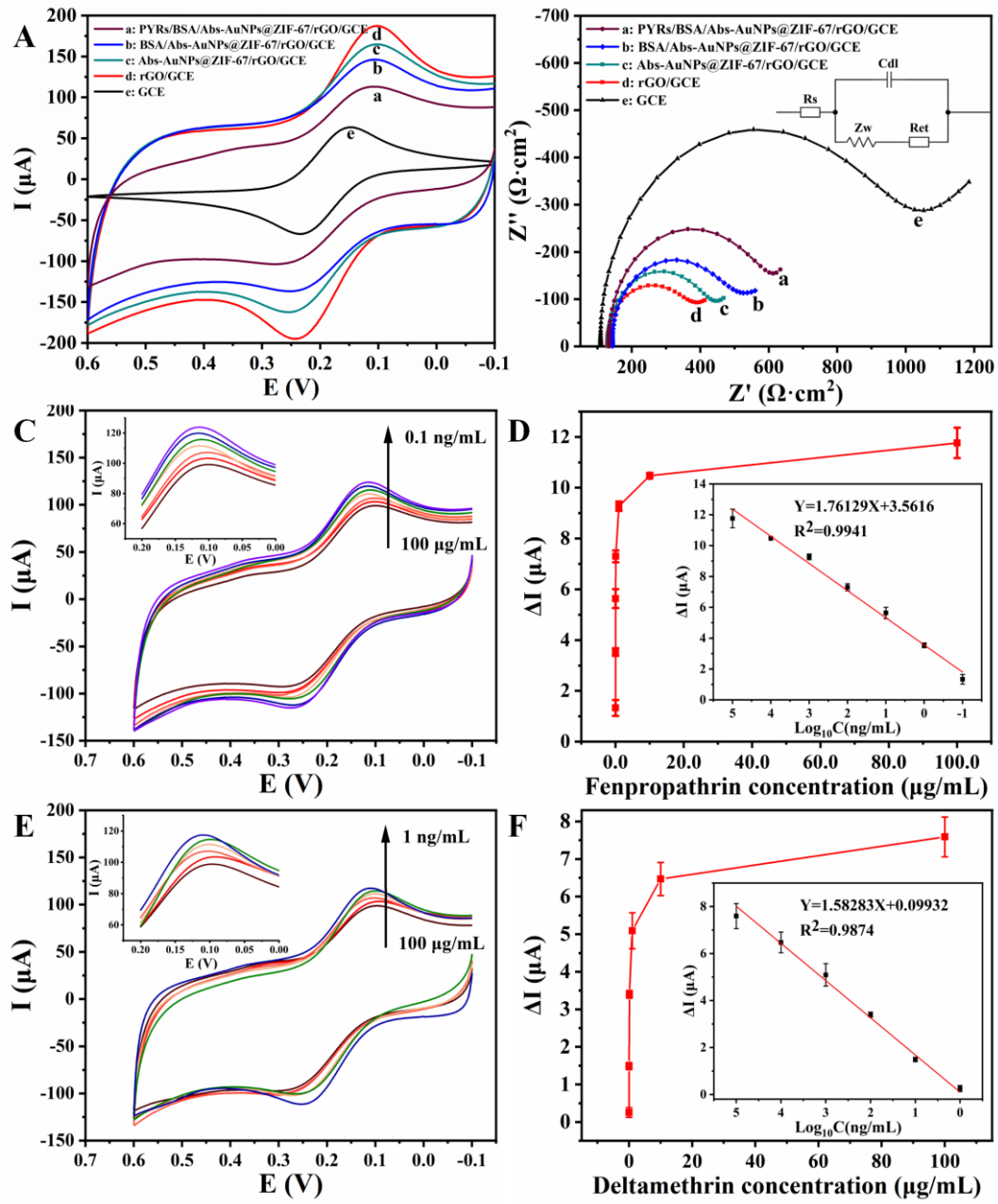

Figure 5. Characterization of different modification steps by CV (A) and EIS (B) in 5.0 mM $[Fe(CN)_6]^{3-/4-}$ containing 0.1 M KCl (pH 7.4). Typical CV curves of the developed sensor in with different concentrations of (C) fenpropathrin (0.1 ng/mL, 1 ng/mL, 10 ng/mL, 100 ng/mL, 1 μg/mL, 10 μg/mL, 100 μg/mL) and (D) deltamethrin (1 ng/mL, 10 ng/mL, 100 ng/mL, 1 μg/mL, 10 μg/mL, 100 μg/mL). The linear relationship between the CV intensity and the logarithm for the concentrations of the fenpropathrin (D) and deltamethrin (F).

Under the optimum working conditions for the electrochemical immunosensor, we investigated the correlation between the PYR concentration (C) and the relative difference of the electrochemical redox peak signal (ΔI). As the concentration of the PYR sample was increased, more PYRs-Abs combinations were bound to the interface of the electrochemical immunosensor, increasing the impedance of the immunosensor surface and weakening the electron transfer ability , thereby increasing ΔI. Figure 5C and Figure 5E show the CV relationship for fenpropathrin and deltamethrin concentrations respectively. Figure 5D and Figure 5F show a linear correlation between ΔI and the logarithms of the fenpropathrin and deltamethrin concentrations, respectively. The linear correlation coefficients (R2) were determined to be 0.9941 and 0.9874, respectively. The linear equations were expressed as ΔI=3.5616+1.76129LogC and ΔI=0.09932+1.58283LogC, respectively. The LOD can be obtained by substituting the mean value (B0) and standard deviation (SD) determined for the negative samples after three tests into the calculation formula (LOD=B0-3*SD). The limits of detection for fenpropathrin and deltamethrin were determined to be 0.009 ng/mL (0.0258 nM) and 0.865 ng/mL (1.712 nM), respectively. The detection ranges for fenpropathrin and deltamethrin were 0.1-1.0 × 10^5 ng/mL (0.286-2.864 × 10^5 nM) and 1.0-1.0 × 10^5 ng/mL (1.979-1.979 ×10^5 nM), respectively.

We compared these parameters with those obtained for other types of sensors, such as electrochemical luminescence sensors (ECL) and surface-enhanced Raman spectroscopy sensors (SERS), as shown in Table 1. The results showed that the electrochemical immunosensor in this manuscript has a wide detection linear range and a low LOD, indicating that this research work has a certain significance and potential.

Table 1. Comparison with other types of electrochemical sensors for PYRs detection

Method	Pesticide	Linear range (nM)	LOD (nM)	Reference
ECL	Permethrin	2.6-4.3 × 10^5	2.9	[9]
SERS	Permethrin	100-2.0 × 10^5	3.5	[37]
SERS	Cyfluthrin	46.052-2.302 × 10^6	0.115	[38]
SERS	Cyfluthrin	0.1-10^4	0.1	[39]
SERS	Cypermethrin	10^3-10^6	10^3	[40]
Electrochemistry	Fenpropathrin	0.286-2.864 × 10^5	0.0258	This work
	Deltamethrin	1.979-1.979 × 10^5	1.712	

3.4 Performance test for the electrochemical immunosensor

The performance of the electrochemical immunosensor was evaluated by the important indices of selectivity, reproducibility and anti-interference. The neonicotinoid pesticides acetamiprid and imidacloprid (Figure 6A-e and 6A-f) and the organophosphorus pesticides probromophos and thionophos (Figure 6A-g and 6A-h) were selected as interfering pesticides to explore the changes in the

electrochemical response signals of sensors for different interfering substances before and after incubation. Figure 6A-j shows the data for a matrix solution in the absence of the target. Figure 6A-c shows the data for a mixture of PYRs (fenpropathrin) and non-PYRs (acetamiprid, imidacloprid, propion, thionophos aquifers). Figure 6A-d shows the data for the mixture of PYRs (deltamethrin) and non-PYRs (acetamiprid, imidacloprid, propion, thionophos aquifers). Figure 6A-i shows the data for the mixture of the standard solutions (fenpropathrin, deltamethrin, acetamiprid, imidacloprid, probromophosphoron, and thionophos). The relatively small ΔI value indicated that it was difficult for the gold probe to bind to these interfering pesticide molecules. Unlike nontarget objects, Figure 6A-a, 6A-b, 6A-c and 6A-d show relatively large ΔI values, which proved that the electrochemical immunosensor had good anti-interference and selectivity abilities. To verify the reproducibility of the constructed electrochemical immunosensor, four electrodes were prepared under the same conditions to detect 6.00 ng/mL and 1.00 μg/mL fenpropathrin and deltamethrin, respectively. The relative deviations (RSD) for the four electrodes were 1.63% and 2.26%, respectively, indicating that the immunosensor performs well in terms of reproducibility (Figure 6B).

The stability of the electrochemical immunosensor was also tested. The prepared immunosensors were stored at 4°C and used for detection at 0 h, 72 h, 168 h and 336 h. The electrochemical signals for the fenpropathrin immunosensor and deltamethrin immunosensor were determined to be 94.83%-99.82% and 83.19%-97.48% of the initial signal, respectively, and the electrochemical immunosensor demonstrated good stability (Figure 6C).

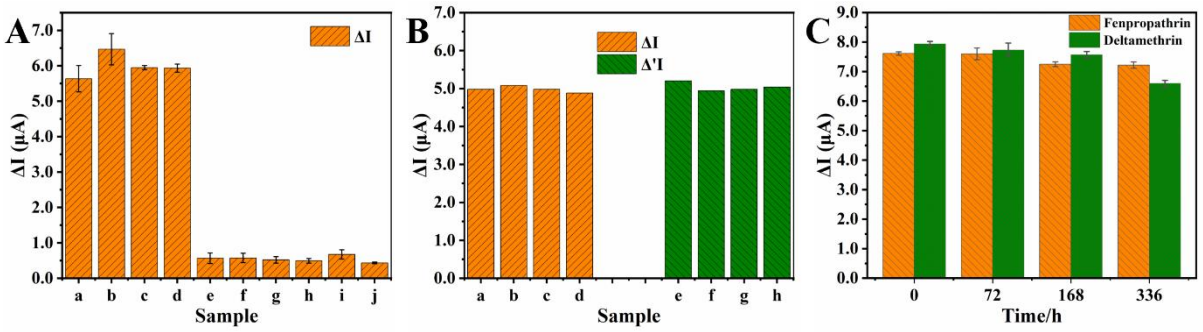

Figure 6. (A) Specificity of the immunosensor. (B) Reproducibility of the immunosensor. (C) Stability of the immunosensor.

3.5 Detection of synthetic PYRs in vegetable samples

To test the detection capability of the constructed electrochemical immunosensor for real samples, we prepared a sample matrix solution containing lettuce and baby cabbage obtained from a supermarket and used it in a detection experiment. The final labelled sample solution was prepared in different concentrations for detection and analysis. The test results obtained for the spiked vegetable sample solution are shown in Table 2. The recoveries ranged from 93.69% to 102.11%, and the relative standard deviations (RSD) ranged from 1.27% to 4.38%. The results show that the electrochemical immunosensor constructed by this method has a high recovery rate and a low RSD. Table 2 shows that the recovery rate

of the constructed electrochemical immunosensor is greater than 90%. The detection results obtained for gas chromatography-mass spectrometry (GC-MS) are shown in Table 3. The results show that the prepared electrochemical immunosensor has high specificity and good repeatability and has great application potential for the detection of PYRs in vegetables.

Table 2. Recovery of the sensor in samples (n=3)

Sample	Pesticides	Added (ng/mL)	Measured quantity (ng/mL)	RSD (%)	Recovery (%)
Lettuce	Fenpropathrin	0	0	-	-
		100.00	93.69	1.85	93.69
		1000.00	1021.07	4.38	102.11
	Deltamethrin	0	0	-	-
		71.70	68.22	1.54	95.15
		717.00	726.83	3.61	101.37
Baby cabbage	Fenpropathrin	0	0	-	-
		100.00	98.73	2.64	98.73
		1000.00	997.12	2.59	99.71
	Deltamethrin	0	0	-	-
		71.70	70.62	1.27	98.49
		717.00	708.93	3.23	98.87

Table 3. Detection results for GC-MS

Samples	Pesticides	Added (ng/mL)	Measured quantity (ng/mL)	RSD (%)	Recovery (%)
Lettuce	Fenpropathrin	0	0	-	–
		100.00	110.21	2.62	110.21
Baby cabbage	Deltamethrin	0	0	-	–
		71.70	76.20	5.30	94.01

4. CONCLUSION

This work constructed a novel electrochemical immunosensor labelled with a broad-spectrum antibody probe by a one-step wet chemistry method for the rapid detection of pyrethroid pesticides in vegetables. First, the Abs-AuNPs@ZIF-67 probe was formed by coupling the PYRs antibody with the a

signal amplification element, AuNPs@ZIF-67. Then, the Abs-AuNPs@ZIF-67 probe was fixed onto the surface of the rGO-modified GCE electrode. This method enhanced the uniform dispersion effect of gold-labelled antibody on the electrode surface and improved the immobilization level for the broad-spectrum antibody. The fenpropathrin and deltamethrin concentrations showed a good correlation with the electrochemical signal under optimal experimental conditions, with linear correlation coefficients of 0.9941 and 0.9874, respectively.The detection ranges for fenpropathrin and deltamethrin were determined to be 0.286-2.864 × 10^5 nM and 1.979-1.979 × 10^5 nM, respectively. The limits of detection for fenpropathrin and deltamethrin were 0.0258 nM and 1.712 nM, respectively. The electrochemical immunosensor was found to show a high recovery rate (93.69%-102.11%) in a spiked sample recovery experiment. The constructed electrochemical immunosensor had high selectivity and stability. This work created a new gold-labelled antibody probes for the rapid detection of PYRs and provided a reference idea for the construction of electrochemical immunosensors for the detection of other pesticides and small molecule targets.

ACKNOWLEDGMENTS
This work was supported by the National Natural Science Foundation of China (31772068, 31872909) and R&D Innovation Project for Major Agriculture Application Technology of Shandong Province (SD2019ZZ023).

References

1. Y. Zhao, D. Du, Q. Li, W. Chen, Q. Li, Q. Zhang and N. Liang, *Microchem. J.*, 159 (2020) 105411.
2. P. Fruhmann, A. Sanchis, L. Mayerhuber, T. Vanka, C. Kleber, J.-P. Salvador and M.-P. Marco, *Anal. Bioanal. Chem.*, 410 (2018) 5923-5930.
3. D.E. Camilo, C.M. Miyazaki, F.M. Shimizu and M. Ferreira, *Mater. Sci. Eng.*, C, 102 (2019) 315-323.
4. E.L. Dávila, M. Houbraken, Z.G. Unday, O.R. Romero, G. Du Laing and P. Spanoghe, *SN Appl. Sci.*, 2 (2020) 1-12.
5. J. Huo, Z. Li, D. Wan, D. Li, M. Qi, B. Barnych, N. Vasylieva, J. Zhang and B.D. Hammock, *J. Agric. Food. Chem.*, 66 (2018) 11284-11290.
6. R.I. Veneciano, V.S. Parra, W. Quiroz, E. Fuentes, L.F. Aguilar and M.A. Bravo, *Microchem. J.*, 159 (2020) 105561.
7. I. Al Yahyai, J. Hassanzadeh and H.A. Al-Lawati, *Sens. Actuators*, B, 327 (2021) 128927.
8. A.Y. El-Moghazy, J. Huo, N. Amaly, N. Vasylieva, B.D. Hammock and G. Sun, *ACS Appl. Mater. Interfaces*, 12 (2020) 6159-6168.
9. Y. Zhao, L. Tian, S. Wu, X. Zhang, Z. Sun, Y. Hu, Y. Wang, R. Chen and J. Lu, *Microchem. J.*, 168 (2021) 106487.
10. V. Vogiazi, A. de la Cruz, S. Mishra, V. Shanov, W.R. Heineman and D.D. Dionysiou, *ACS Sens.*, 4 (2019) 1151-1173.
11. L. Hou, X. Zhang, Y. Huang, M. Wang, X. Chen, T. Lin, Y. Tan and S. Zhao, *J. Pharm. Biomed. Anal.*, (2021) 114400.
12. J. Bao, T. Huang, Z. Wang, H. Yang, X. Geng, G. Xu, M. Samalo, M. Sakinati, D. Huo and C. Hou, *Sens. Actuators*, B, 279 (2019) 95-101.
13. J. Fu, X. An, Y. Yao, Y. Guo and X. Sun, *Sens. Actuators*, B, 287 (2019) 503-509.
14. Y. Zhao, H. Zeng, X.-W. Zhu, W. Lu and D. Li, *Chem. Soc. Rev.*, (2021).

15. L. Zhang, Y. Mazouzi, M. Salmain, B. Liedberg and S. Boujday, *Biosens. Bioelectron.*, 165 (2020) 112370.
16. S. Zhou, J. Hu, X. Chen, H. Duan, Y. Shao, T. Lin, X. Li, X. Huang and Y. Xiong, *Anal. Chim. Acta*, 1168 (2021) 338623.
17. M. Li and B. He, *Sens. Actuators*, B, 329 (2021) 129158.
18. X. Chen, J.-X. Zhao, J.-W. Wang, Y. Liu, L.-C. Wang, R. Weerasooriya and Y.-C. Wu, *Electrochim. Acta*, 387 (2021) 138539.
19. W. Meng, Y. Wen, L. Dai, Z. He and L. Wang, *Sens. Actuators,* B, 260 (2018) 852-860.
20. S.P. Selvam, A.N. Kadam, K.R. Maiyelvaganan, M. Prakash and S. Cho, *Biosens. Bioelectron*., 187 (2021) 113302.
21. J.Y.R. Silva, Y.G. Proenza, L.L. da Luz, S. de Sousa Araújo, M.A. Gomes Filho, S.A. Junior, T.A. Soares and R.L. Longo, *Mater. Sci. Eng.*, C, 102 (2019) 578-588.
22. L. Xu, Y. Xiong, B. Dang, Z. Ye, C. Jin, Q. Sun and X. Yu, *Mater. Des.*, 182 (2019) 108006.
23. R.M. Abdelhameed, M. Abu-Elghait and M. El-Shahat, *J. Environ. Chem. Eng.*, 8 (2020) 104107.
24. W. Cui, X. Kang, X. Zhang, Z. Zheng and X. Cui, *Physica E*, 113 (2019) 165-171.
25. L. Liu, Y.-j. Hao, Z. Li, C. Chen, M.-y. Wu and S. Feng, *Chem. Pap.*, 74 (2020) 1839-1847.
26. X. Liu, W. Chen, M. Lian, X. Chen, Y. Lu and W. Yang, *J. Electroanal. Chem*., 833 (2019) 505-511.
27. J. Hu, G. Kong, Y. Zhu and C. Che, *Chin. Chem. Lett.*, 32 (2021) 543-547.
28. P. Dai, Y. Yao, E. Hu, D. Xu, Z. Li and C. Wang, *Appl. Surf. Sci.,* 546 (2021) 149128.
29. G. He, Y. Li, L. Wu, Y. Wang, M. Liu, J. Yuan and X. Men, *Tribol. Int*., 161 (2021) 107091.
30. H. Dong, Q. Zhao, J. Li, Y. Xiang, H. Liu, Y. Guo, Q. Yang and X. Sun, *Bioprocess. Biosyst. Eng.*, 44 (2021) 585-594.
31. F.-Y. Qiao, J. Liu, F.-R. Li, X.-L. Kong, H.-L. Zhang and H.-X. Zhou, *Appl. Surf. Sci.*, 254 (2008) 2941-2946.
32. T.H.L. Nghiem, T.H. La, X.H. Vu, V.H. Chu, T.H. Nguyen, Q.H. Le, E. Fort, Q.H. Do and H.N. Tran, *Adv. Nat. Sci.: Nanosci. Nanotechnol*., 1 (2010) 025009.
33. G. Surekha, K.V. Krishnaiah, N. Ravi and R.P. Suvarna, *J. Phys. Conf. Ser.*, 2020, pp. 012012.
34. P. Sengunthar, K. Bhavsar, C. Balasubramanian and U. Joshi, *Appl. Phys. A,* 126 (2020) 1-9.
35. C. Ye, X. Chen, D. Zhang, J. Xu, H. Xi, T. Wu, D. Deng, C. Xiong, J. Zhang and G. Huang, *Electrochim. Acta*, 379 (2021) 138174.
36. H. Zhao, T. Liu, L. Cui, Y. Li, F. Yang and X. Zhang, *Sens. Actuators*, B, (2021) 130332.
37. T.B. Pham, T.H.C. Hoang, V.H. Pham, T. Van Nguyen, D.C. Vu and H. Bui, *Sci. Rep.*, 9 (2019) 1-10.
38. J. Xu, R. Zhang, C. Liu, A. Sun, J. Chen, Z. Zhang and X. Shi, *Sensors.*, 20 (2020) 884.
39. Y. Wang, H. Li, X. Wang, Z. Wang, M. Wang, Y. Li and Q. Wang, *J. Raman Spectrosc*., 50 (2019) 926-935.
40. W. Leung, S. Limwichean, N. Nuntawong, P. Eiamchai, S. Kalasung, O.-U. Nimittrakoolchai and N. Houngkamhang, *Key Eng. Mater.*, 2020, pp. 102-106.